

Lattice dynamics of xenotime: The phonon dispersion relations and density of states of LuPO₄

J. C. Nipko and C.-K. Loong

Argonne National Laboratory, Argonne, Illinois 60439-4814

M. Loewenhaupt

Technische Universität Dresden, Dresden, Germany

M. Braden and W. Reichardt

Forschungszentrum Karlsruhe, INFP, D-76021, Karlsruhe, Germany

L. A. Boatner

Oak Ridge National Laboratory, Oak Ridge, Tennessee 37831-6056

(Received 19 May 1997; revised manuscript received 21 July 1997)

LuPO₄ is the nonmagnetic end member of a series of rare-earth phosphates with a common zircon-type crystal structure. The phonon-dispersion curves of LuPO₄ along the $[x,0,0]$, $[x,x,0]$, and $[0,0,x]$ symmetry directions were measured by neutron triple-axis spectroscopy using single-crystal samples. The phonon density of states was determined by time-of-flight neutron scattering using polycrystalline samples. Phonons involving mainly motions of rare-earth ions were found to be well separated in energy from those of the P and O vibrations. A large gap in the phonon-frequency-distribution function, which divides the O-P-O bending-type motions from the P-O stretches, was observed. All of the experimental results were satisfactorily accounted for by lattice-dynamic shell-model calculations. LuPO₄ is a host material for the incorporation of rare-earth ions to produce activated luminescence. Information regarding the phonon and thermodynamic properties of LuPO₄ is pertinent to extended investigations of additional rare-earth spin-lattice interactions in other zircon-structure rare-earth orthophosphates. [S0163-1829(97)06741-6]

I. INTRODUCTION

LuPO₄ crystallizes in the zircon structure, which is common to a variety of optical materials, including the natural minerals zircon (ZrSiO₄) and xenotime (RPO₄, R = Y, Tb to Lu, and Sc), as well as rare-earth vanadates and arsenates. Zircon variants with impurities of actinide or transition-metal ions occupying the Zr sites are also found in plutonic igneous rocks. The high melting temperatures, structural, and chemical stability, radiation-damage resistance, and long-term corrosion resistance of zircon and the rare-earth orthophosphates has led to investigations of their use as a nuclear-waste storage medium. Information regarding the phonon properties is relevant to achieving an understanding of the thermodynamic behavior of these materials under natural radiation-damage and temperature-pressure conditions prevalent in the earth.

Zircon-type crystalline hosts, in general, exhibit good optical quality (refractive index of 1.8–2.0, birefringence of 0.04–0.10), and phonons play a vital role in the luminescence properties of transition-metal-doped crystals.¹ For example, the charge-transfer-type luminescence of Yb³⁺ and Sb³⁺ ions in RPO₄ (R = Sc, Lu, and Y) indicates vibronic coupling involving phonons of energies of about $270 \pm 30 \text{ cm}^{-1}$ ($34.1 \pm 3.7 \text{ meV}$).² The cooperative Jahn-Teller phase transitions in several stoichiometric rare-earth phosphates and vanadates, which involve coupling of the rare-earth crystal-field-split states with acoustic or low-lying optic phonons, have been investigated by Raman scattering and infrared absorption.^{3,4} More recently, a neutron-scattering

study showed evidence of interactions of $4f$ electrons and acoustic phonons in TmVO₄ at finite wave vectors.⁵

The high-energy ($> 100 \text{ meV}$) optic phonons that mainly involve vibrations of the P and O atoms are important in their own right. The frequencies and widths of these phonon bands reflect the nature of the connectivity and bonding of PO₄ tetrahedra in the lattice. In rare-earth orthophosphates the PO₄ units are not directly connected, and the P-O stretch frequencies lie within a narrow range of 120–135 meV. In condensed pyro-, meta-, and ultraphosphates, on the other hand, corner-sharing PO₄ tetrahedra form dimers, chainlike, and network structures, respectively, and the P-O stretch frequencies progressively increase to $\sim 160 \text{ meV}$ with wider band widths.⁶ Without modifying metal cations, the branching configuration, where three O atoms of a PO₄ unit are shared with three neighboring PO₄ in phosphorus pentoxide, is inherently unstable due to the unbalanced distribution of oxygen $d\pi$ phosphorous $p\pi$ bonding character over the P-O bonds. This forms the basis for the antibranching rule proposed by Van Wazer.⁷ Thus far, the P-O stretch vibrational density of states of various phosphate crystals or glasses have not been determined. Only the zone-centered modes of RPO₄ and ZrSiO₄ compounds were measured by optical spectroscopy.^{8–15}

In this paper, we report on the determination of the phonon-dispersion curves and phonon density of states (DOS) of LuPO₄ obtained by neutron scattering using single-crystal and polycrystalline samples. This compound was chosen for the initial investigations because Lu³⁺ ions have a completely filled $4f$ shell carrying no net magnetic moment.

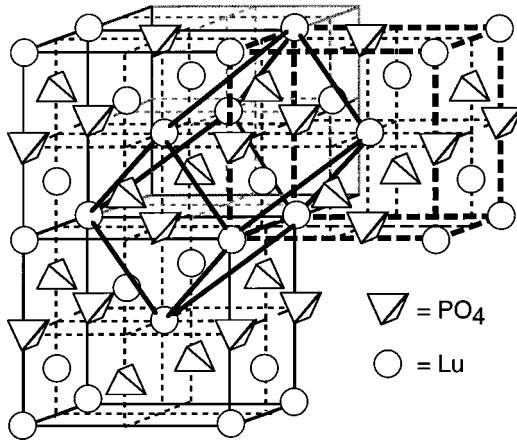


FIG. 1. The zircon structure of LuPO_4 . The individual PO_4 units are shown schematically by tetrahedra. The two sets of dashed lines and heavy lines outline the body-centered-tetragonal unit cell and the primitive cell, respectively.

The phonon spectrum of LuPO_4 may, therefore, be used as a gauge for nonmagnetic $R\text{PO}_4$ hosts of orthophosphates.

II. GROUP-THEORETICAL ANALYSIS

Only Raman and infrared data exist for a few of the zircon-structure compounds. Previous group-theoretical analysis of the vibrational modes was restricted to zone-centered modes for the interpretation of the optical data.^{14,16} Here we present a group-theoretical analysis for the zircon structure along major symmetry directions in the Brillouin zone. The body-centered-tetragonal unit consists of four formula units of LuPO_4 . A primitive cell can be chosen with only two formula units, resulting in 36 phonon branches. The tetragonal unit cell and the primitive cell are displayed in Fig. 1, schematically showing the individual PO_4 tetrahedra in the lattice. The crystallographic space group (No. 141) is $D_{4h}^{19}(I4_1/amd)$. The crystal structure exhibits a point symmetry of $D_{2d}(4m2)$ at the Lu and P sites with a uniaxial direction along the c axis, while the oxygen atoms occupy sites of $C_{1h}(m)$ symmetry.¹⁷ In this structure, eight O atoms are coordinated to the central Lu atom forming two interpenetrating tetrahedra, each of which is characterized by a unique P-O distance. A distorted triangulated dodecahedron is formed by connecting the oxygen vertices, see Fig. 2. The principal structure can be considered as a chain of alternating edge-sharing PO_4 tetrahedra and RO_8 triangular dodecahedra extending parallel to the c axis, with the chain joined laterally by edge-sharing RO_8 dodecahedra. The bond lengths, bond angles, and atomic positions within the primitive cell are given in Table I.

The Brillouin zone of the body-tetragonal structure for LuPO_4 ($a > c$) are shown in Fig. 3. The three symmetry directions, Δ , Σ , and Λ correspond in Cartesian coordinates to the $[x, x, 0]$, $[x, 0, 0]$, and $[0, 0, x]$ directions, respectively. The symmetry decomposition of the phonon modes along various symmetry points and directions in the Brillouin zone, derived from standard group theory,¹⁸ are given in Table II. The compatibility relations between the Γ point and the Δ , Σ , and Λ lines are given in Table III.

It has been observed that condensed phosphates having an

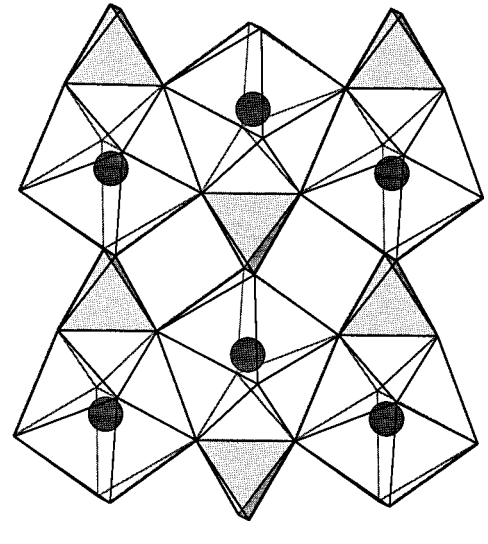


FIG. 2. The arrangement of PO_4 tetrahedra and RO_8 triangular dodecahedra in LuPO_4 .

ionic complex such as PO_4^{-3} often exhibit localized modes that are due essentially to internal vibrations of the atoms of the PO_4 species. Therefore, it is instructive to explore the symmetry relations between $\text{Lu} \cdot (\text{PO}_4)$ where the PO_4 unit is treated as rigid molecules and an isolated PO_4 molecule. The reducible representation of the vibrational modes of a free PO_4 unit of T_d symmetry decomposes according to $T_d \rightarrow A_1 + E + F_1 + 3F_2$. The internal modes labeled using Herzberg's notations¹⁹ are: ν_1 (A_1 , symmetric stretching), ν_2 (E , bond bending), ν_3 (F_2 , antisymmetric stretching), and ν_4 (F_2 , bond bending). The other F_2 and the F_1 modes are external modes corresponding to pure rotation and pure translation of the PO_4 unit, respectively. In LuPO_4 , the point symmetry of the PO_4^{-3} units is D_{2d} , which is lower than T_d , and the modes split according to: $A_1 \rightarrow A_1$, $E \rightarrow A_1 + B_1$, $F_1 \rightarrow A_2 + E$, $3F_2 \rightarrow 3B_2 + 3E$. Since there are two PO_4^{-3} complexes within the primitive unit cell, there are twice as many modes of each species. In the absence of an interaction between the two molecules in the primitive cell, these pairs of modes would be degenerate. In the crystal, the extent of splitting of these modes gives an indication of the strength of coupling to the environment.

The symmetry of the vibrational modes of $\text{Lu} \cdot (\text{PO}_4)$, where the Lu atoms and rigid PO_4 molecules are under point symmetry D_{2d} , reduces to $4A_1 + 2B_1 + 2A_2 + 8B_1 + 10E$. They can be further related to the D_{4h} symmetry of the crystal if we consider that the motion of the Lu^{3+} ions under D_{2d} symmetry will transform according to B_2 and E for translations along the c axis and in the a - b plane, respectively. The decomposition follows as: $4A_1 \rightarrow 2A_{1g} + 2B_{2u}$, $2B_1 \rightarrow B_{1g} + A_{1u}$, $2A_2 \rightarrow A_{2g} + B_{1u}$, $6B_2 + 2B_2 \rightarrow 4B_{2g} + 4A_{2u}$, $8E + 2E \rightarrow 5E_g + 5E_u$. The correlation between mode symmetries is easily seen if we consider the nature of the modes. For example, the A_{1g} and B_{2u} modes under D_{4h} symmetry are related by the inversion operator, the A_{1g} corresponding to 180° out-of-phase motions of the two molecules of LuPO_4 and the B_{2u} corresponding to in-phase motions. Therefore, the correspondence between the four A_1 modes of D_{2d} and the $2A_{1g}$ and $2B_{2u}$ modes is a natural consequence. In a

TABLE I. The structural parameters for LuPO₄ at 10 K. The space group for this structure is $I 4_1/amd$. $a=6.7915(2)$ Å and $c=5.9544(2)$ Å. Lu atoms occupy the a sites, P atoms occupy the b sites, O atoms occupy the h sites. The oxygen fractional position parameters are $x=0.4270(2)$ and $z=0.2151(2)$.

Atom type	Cartesian components		
	X	Y	Z
Lu ₁	0	0	0
Lu ₂	0	1/2	1/4
P ₁	0	0	1/2
P ₂	0	1/2	-1/4
O ₁	0	$x-1/2$	$z+1/8$
O ₂	0	$-x+1/2$	$z+1/8$
O ₃	0	$x+1/4$	$-z+1/8$
O ₄	0	$-x+3/4$	$-z+1/8$
O ₅	$x-1/4$	0	$-z+7/8$
O ₆	$-x+1/4$	0	$-z+7/8$
O ₇	$x-1/4$	1/2	$z-5/8$
O ₈	$-x+1/4$	1/2	$z-5/8$

Bond type	Distance (Å)
P ₁ -O ₁	1.534
Lu ₁ -O ₁	2.258
Lu ₁ -O ₄	2.354
O ₁ -O ₂	2.404
O ₁ -O ₅	2.553
O ₁ -O ₄	2.745
O ₁ -O ₈	2.910
Bond angle	
O ₁ -P ₁ -O ₂	112.62°
O ₁ -P ₁ -O ₅	103.33°
O ₁ -Lu ₂ -O ₂	152.49°
O ₁ -Lu ₁ -O ₂	61.47°

similar way, we can derive the correlations between the remaining modes. In Table IV we summarize the results of the symmetry analysis.

The selection rules for infrared and Raman measurements of the zone-center modes are: Raman: $2A_{1g}(\alpha_{xx} + \alpha_{yy}, \alpha_{zz}) + 4B_{1g}(\alpha_{xx} - \alpha_{yy}) + B_{2g}(\alpha_{xy}) + 5E_g(\alpha_{yz}, \alpha_{zx})$; IR: $3A_{2u}(E \parallel c \text{ axis}) + 4E_u(E \perp c \text{ axis})$. In the analysis of the neutron data near the zone center, it is important to seek internal consistency with the optical data. The experimental infrared results of Armbruster⁸ and the Raman measurements of Becker⁹ are summarized in Table V.

III. EXPERIMENTAL DETAILS

A detailed investigation of the dynamics of LuPO₄ by neutron scattering requires an approach that combines measurements from a triple-axis spectrometer at a reactor source and a time-of-flight instrument from a spallation source. The highly dispersive and densely spaced phonon branches below 80 meV can be effectively studied by triple-axis measurements using single crystals. Combining the knowledge of the

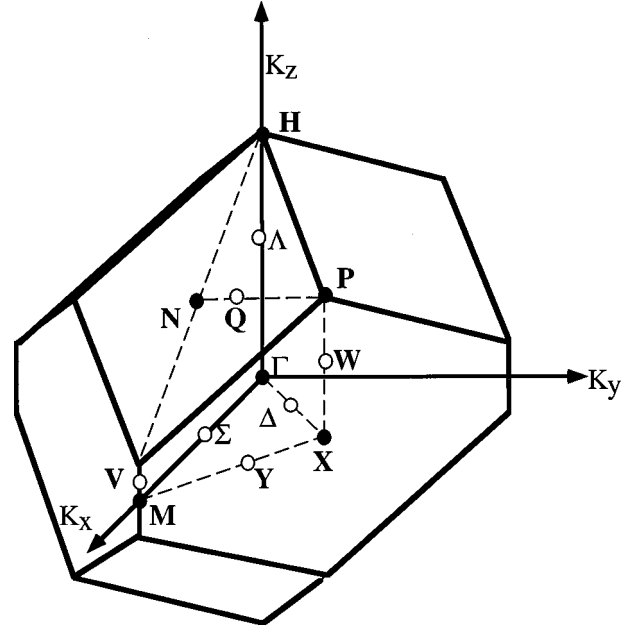


FIG. 3. The Brillouin zone for a body-centered-tetragonal system with $a > c$. The high-symmetry points and lines are indicated with conventional group-theoretical notation. The Cartesian coordinates for the zone-boundary points Δ , Σ , and Λ are $[\pi/a, \pi/a, 0]$, $[2\pi/a, 0, 0]$, and $[0, 0, \pi/c(1 + (c/a)^2)]$, respectively.

phonon-symmetry relations with the flexibility of constant- Q and constant- E operations provided by a triple-axis spectrometer allows quantitative measurements of the frequencies and neutron-group intensities of individual phonon branches up to about 80 meV. This information is crucial to

TABLE II. Symmetry decomposition for the high-symmetry points and lines.

Symmetry points:	
$\Gamma(D_{4h})$	$\rightarrow 2A_{1g} + A_{1u} + A_{2g} + 4A_{2u} + 5E_g + 5E_u + 4B_{1g} + B_{1u} + B_{2g} + 2B_{2u}$
$M(D_{4h})$	$\rightarrow 2A_{1g} + A_{1u} + A_{2g} + 4A_{2u} + 5E_g + 5E_u + 4B_{1g} + B_{1u} + B_{2g} + 2B_{2u}$
$X(D_{2h})$	$\rightarrow 3A_g + 5B_{1g} + 5B_{2g} + 5B_{3g} + 3A_u + 5B_{1u} + 5B_{2u} + 5B_{3u}$
$P(D_{2d})$	$\rightarrow 3A_1 + 3A_2 + 5B_1 + 5B_2 + 10E$
$N(C_{2h})$	$\rightarrow 11A_g + 7A_u + 7B_g + 11B_u$
Symmetry lines:	
$\Lambda(C_{4v})$	$\rightarrow 6A_1 + 2A_2 + 10E + 6B_1 + 2B_2$
$V(C_{4v})$	$\rightarrow 6A_1 + 2A_2 + 10E + 6B_1 + 2B_2$
$\Sigma(C_{2v})$	$\rightarrow 11A_1 + 7A_2 + 11B_1 + 7B_2$
$\Delta(C_{2v})$	$\rightarrow 8A_1 + 8A_2 + 10B_1 + 10B_2$
$W(C_{2v})$	$\rightarrow 8A_1 + 8A_2 + 10B_1 + 10B_2$
$Y(C_{2v})$	$\rightarrow 8A_1 + 8A_2 + 10B_1 + 10B_2$
$Q(C_2)$	$\rightarrow 18A + 18B$

TABLE III. Compatibility relations between the Γ point and the high-symmetry lines.

Γ point	Σ line (100)	Λ line (001)	Δ line (110)
A_{1g}	A_1	A_1	A_1
A_{1u}	A_2	A_2	A_2
A_{2g}	B_2	A_2	B_1
A_{2u}	B_1	A_1	B_2
E_g	$A_2 + B_1$	E	$A_2 + B_2$
E_u	$A_1 + B_2$	E	$A_1 + B_1$
B_{1g}	A_1	B_1	B_1
B_{1u}	A_2	B_2	B_2
B_{2g}	B_2	B_2	A_1
B_{2u}	B_1	B_1	A_2

model fitting. On the other hand, the weakly dispersive high-energy modes associated mainly with P-O motions can be determined effectively using epithermal neutrons from polycrystalline samples and time-of-flight methods.

Measurements on a single crystal of LuPO_4 (about 0.75 cm^3 in size) were performed using the 2T1 triple-axis spectrometer at the Laboratoire Leon Brillouin in Saclay, France. The crystal was synthesized by a flux-growth technique described previously.²⁰ Below 40 meV, the scattering from the (002) planes of pyrolytic graphite (PG) were used for monochromator and analyzer. Above 40 meV, copper (111) and PG (002) were used as monochromator and analyzer, respectively. Both the monochromator and analyzer consist of horizontally and vertically focusing crystal arrays for maximizing intensity while maintaining an adequate resolution. The scans were conducted with a fixed final neutron energy of 14.7 or 30.5 meV in conjunction with the use of a PG filter in the scattered beam to suppress higher-order contaminations. The crystal was cooled by a close-cycle helium refrigerator and kept at 15 K throughout the measurements. A majority of the phonon branches along the $[x,0,0]$, $[x,x,0]$, and $[0,0,x]$ symmetry directions were measured with the sample oriented so that the scattering wave vectors are in either the $(h0k)$ or $(hk0)$ planes. Assignments of the observed excitation frequencies to phonon branches were guided by self-consistency checks of the neutron-group intensities against the structure factors from model calculations.

The time-of-flight experiments were performed using the High-Resolution Medium-Energy Chopper Spectrometer (HRMECS) at the Intense Pulsed Neutron Source (IPNS) of Argonne National Laboratory. A polycrystalline sample of LuPO_4 ($\sim 60 \text{ g}$) was prepared by the coprecipitation of lutetium oxide and ammonium hydrogen phosphate in molten urea followed by a calcination at 800°C to remove the urea.²¹ The powder sample was then pressed into pellets and annealed at 1200°C in air for 24 h, since such heat treatments are known to promote grain growth and improve the crystalline quality. The annealed sample was then characterized by neutron powder diffraction at IPNS and found to be the single-phase zircon structure—in good agreement with the reported structure in the literature¹⁷ (with a typical weighted R factor of 5% in a Rietveld analysis).

The HRMECS spectrometer is equipped with wide-angle

multidetector banks which, using an incident neutron energy (E_0) of 200 meV, allow measurements of inelastic scattering over a wide range of momentum and energy transfer. The energy resolution ΔE in full width at half maximum of the HRMECS spectrometer varies from approximately 4% of E_0 in the elastic region to $\sim 2\%$ near the end of the neutron-energy-loss spectrum. The powder was contained in an aluminum planar cell mounted at a 45° angle to the incident neutron beam. Such a geometry decreases the neutron traverse length in the sample to $< 5 \text{ mm}$ for all detector angles—thereby reducing multiple-scattering effects. Multiple scattering was estimated to be less than 5% of the total measured intensity and was corrected by removing a small, flat background from the data. To reduce multiple-phonon excitations, the samples were cooled to 15 K for the experiments. Normal background scattering was subtracted from the data by using empty-container runs. Measurements of elastic incoherent scattering from a vanadium standard provided detector calibration and intensity normalization.

IV. EXPERIMENTAL RESULTS AND ANALYSIS

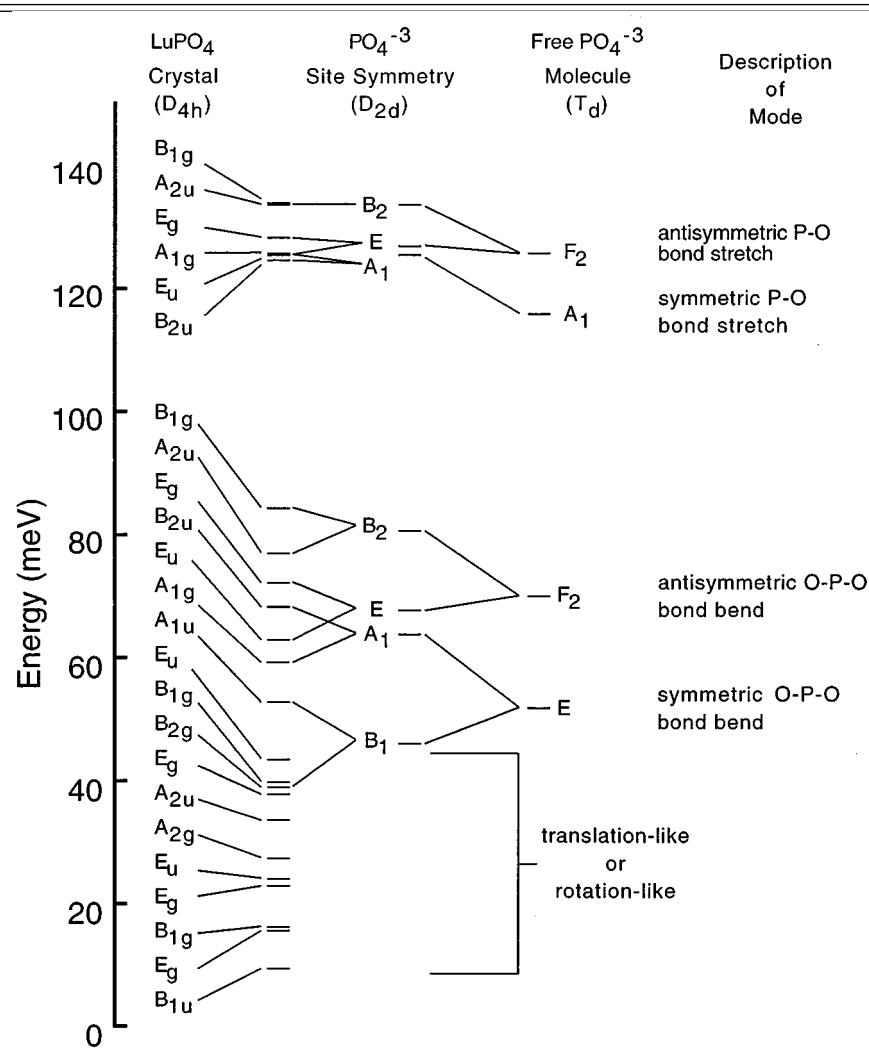
A. Phonon-dispersion curves

The measured phonon-dispersion curves of LuPO_4 at 10 K along the $[x,0,0]$, $[x,x,0]$, and $[0,0,x]$ symmetry directions are shown in Fig. 4. They are labeled according to the irreducible representations (see Table II). The zone-center Raman frequencies reported by P. C. Becker,⁹ as well as, IR frequencies reported by Armbruster⁸ are also plotted in Fig. 4. It can be seen that the acoustic branches are confined to rather low energies, $\sim 20 \text{ meV}$ for longitudinal and $\sim 10 \text{ meV}$ for transverse modes, due to strong interactions with the next optic branches. There is a large phonon gap in the 85–115 meV region.

B. Lattice-dynamics calculations

There are a number of key elements pertaining to the structure and bonding in LuPO_4 that need to be considered in developing a model for this system. First, the nearest-neighbor (NN) P-O bonds are part of a tightly bound PO_4 tetrahedron resulting from sp^3 hybridization of the P outer orbitals forming directional σ bonds with the O atoms. This hybridization favors the PO_4 tetrahedra. The remaining electron of P is presumably transferred to ionic bonding of the PO_4^{3-} with the Lu^{3+} ions. The importance of this structure is illustrated by the gap in the phonon frequency spectrum between ~ 85 – 150 meV . Above 115 meV, the modes consist principally of P-O bond-stretching within the tightly bound PO_4 units. Second, the effects of ionicity can be seen in the neutron and IR data as large splittings of the polar optic modes. For example, the observed frequency of each of the three A_{2u} modes, depending on the propagation direction, shift by as much as 16 meV.⁸ Our neutron-scattering results indicate a splitting of 13 meV for the lowest energy A_{2u} optic mode near 33.0 meV. Evidence for the LO-TO splitting of the E_u modes was also seen in both the neutron and IR data. Therefore, the macroscopic electric field characteristic of Coulomb interactions has to be taken into account by the model. Moreover, according to IR absorption data,⁸ the dielectric constants ϵ_0 and ϵ_∞ are 8.8 ± 0.2 and 3.02 ± 0.01 for

TABLE IV. Correlation for symmetry species of the T_d group of the PO_4^{-3} free ion, the D_{2d} group of the Lu^{3+} and PO_4^{-3} sites in the LuPO_4 crystal, and the D_{4h} group of the whole crystal.



the A_{2u} modes ($E \parallel c$ axis) and 7.5 ± 0.2 and 2.82 ± 0.01 for E_u modes ($E \perp c$ axis). The large values of ϵ_∞ are due to the substantial electronic polarizability of the O p orbital. It is clear that a rigid-ion model, which ignores the contribution from the electronic polarizability, would not adequately account for the dielectric properties of this system, since the rigid-ion model would predict $\epsilon_\infty = 1$.

Following the ideas outlined above, a shell model using Born-von Karman-type axially symmetric forces and polarizable oxygen ions was constructed for LuPO_4 . In this model, we have allowed for NN P-O interactions and the nearest- and next NN interactions for the Lu-O and O-O bonds. Summation of the long-range coulomb forces was performed using the Ewald method. The electronic polarization of the O ions is modeled by a shell charge surrounding a core charge at the O nucleus and a shell-core force constant. The dynamic matrix at the Γ point and along the three symmetry directions was block diagonalized using matrices constructed by the projection-operator method.

The solution of the eigenvalue problem and the fitting of the neutron data were carried out using the computer program GENAX. Optimization of the model parameters was

governed by criteria so as to (i) minimize deviation between the calculated frequencies and the observed phonons from neutron and optical data; (ii) minimize the internal pressure and forces acting on the atoms in their equilibrium positions to ensure the correct structure; and (iii) maintain qualitative agreement between the calculated structure factors and measured neutron group intensities. Based on these criteria, we obtained the optimized parameter set given in Table VI.

A comparison of the calculated phonon-dispersion curves with the experimental data is shown in Fig. 4. The modes that belong to different representations are plotted separately in this figure. The agreement between the experimental data points and calculated phonon curves along all three symmetry directions Σ , Δ , and Λ is excellent. Qualitative agreement was also achieved between the measured neutron group intensities and the corresponding calculated inelastic structure factors. The calculated acoustic frequencies in the long-wavelength limit were used to determine the elastic constants, which can be compared with the experimental values obtained by Brillouin-scattering techniques.²² The agreement, as shown in Table VII, is good, with discrepancies limited to about 10% in all elastic constants. The overall

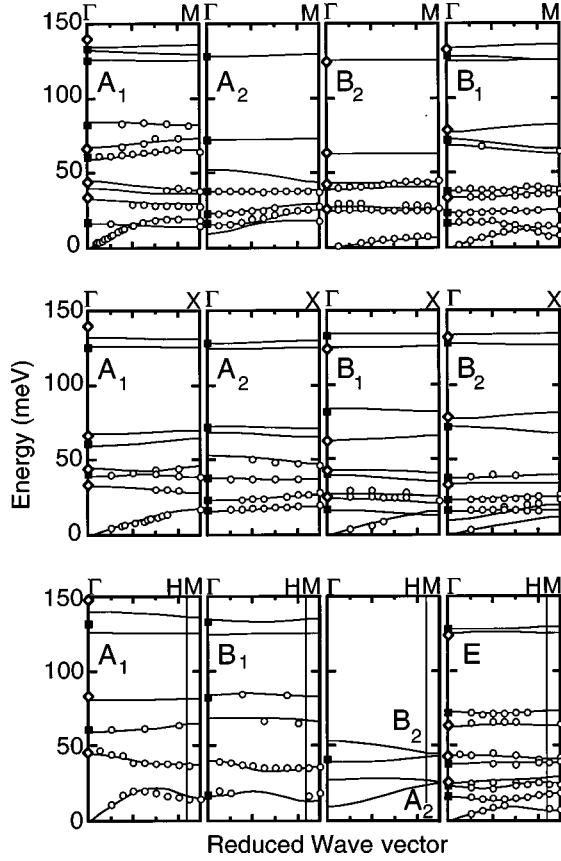


FIG. 4. Phonon-dispersion curves of LuPO_4 along the $[x,0,0]$, $[x,x,0]$, and $[0,0,x]$ symmetry directions. The symbols (\blacksquare = Raman, \blacklozenge = Infrared, and \circ = neutron) indicate observed data, while the lines are calculated curves using the model. Experimental error bars are comparable to the size of the symbols.

agreement between the model predictions and the neutron and optical data (see Table V) leads us to believe that the model with its associated parameters is quite acceptable for the present studies.

C. Phonon density of states

The time-of-flight data collected with an incident neutron energy of 200 meV and scattering angles of 70° to 120° were analyzed. In this configuration, the measured wave vectors Q are between 11 and 20 \AA^{-1} which is much larger than the dimension of the Brillouin zone ($\sim 1 \text{ \AA}^{-1}$) of the crystal reciprocal lattice. Furthermore, the polycrystalline sample effectively provides an average over all crystallographic orientations. Under these conditions, a generalized phonon DOS can be obtained from the measured scattering function $S(Q, E)$ according to^{23–25}

$$G(E) = \frac{2M}{\hbar^2} \left\langle \frac{e^{2W(Q)}}{Q^2} \frac{E}{n(E)+1} S(Q, E) \right\rangle \approx M \sum_i \frac{c_i \sigma_i}{M_i} F_i(E), \quad (1)$$

where c_i , σ_i , M_i , and $F_i(E)$ are the concentration, neutron-scattering cross section, the mass and partial phonon DOS, respectively, for the i th atomic species. M is a mean sample

TABLE V. A comparison of infrared and Raman data (Ref. 8) with model calculation for LuPO_4 .

Mode symmetry	Measured frequency (meV)	Model calculation (meV)
Raman:		
E_g	16.5	16.1
B_{1g}	17.4	16.7
E_g	23.2	23.4
E_g	38.1	38.3
B_{2g}	40.9	39.5
A_{1g}	60.7	59.7
E_g	72.3	72.7
B_{1g}	82.6	84.7
A_{1g}	125.6	126.2
E_g	128.2	128.6
B_{1g}	132.9	134.3
Infrared:		
A_{2u} LO	46.1	45.0
A_{2u} TO	33.0	34.2
A_{2u} LO	83.4	80.9
A_{2u} TO	78.6	77.5
A_{2u} LO	147.8	140.0
A_{2u} TO	131.7	134.0
E_u LO	33.8	33.1
E_u TO	25.7	24.6
E_u LO	44.4	44.9
E_u TO	43.0	43.8
E_u LO	66.6	67.6
E_u TO	64.1	63.3
E_u LO	139.5	132.3
E_u TO	124.0	125.7

mass, $n(E)$ is the Bose-Einstein distribution function, and $\langle \dots \rangle$ represents the average over all observed Q values. The Debye-Waller factors, $e^{-2W(Q)}$ was estimated to be $e^{-0.003 \cdot Q^2}$ in the present case based on the diffraction data. It can be seen from Eq. (1) that $G(E)$ provides a measure of the phonon DOS weighted by the $c_i \sigma_i / M_i$ factors, which is often referred to as the neutron-weighted phonon density of states.

Using the shell model and the optimized parameter set (Table VI), the total and partial phonon DOS of LuPO_4 were computed by a root-sampling method by which the frequency-distribution functions were summed over 343 000 mesh points within the Brillouin zone. Figure 5 shows the calculated phonon DOS as well as the partial DOS for each atom. The generalized one-phonon DOS was evaluated according to Eq. (1) and convoluted with the resolution function of the HRMECS instrument, and the two-phonon contribution was obtained from a self-convolution of the generalized one-phonon DOS. They are plotted in the upper panel of Fig. 6, and the sum is compared with the observed $G(E)$ in the lower panel. The calculated spectrum reproduces all the main features of the observed $G(E)$ over the entire energy range. However, the calculated phonon bands have narrower widths than those observed experimentally. This is perhaps not surprising since the model assumes a

TABLE VI. The parameter set for the shell model. F and G are the axially symmetric force constants for the radial and tangential components, respectively. Charges for the ions and shells are in the unit of $(+e)$.

Bond type	Bond length (Å)	$F(r)$ (10^3 dyn/cm 2)	$G(r)$ (10^3 dyn/cm 2)
Born von Kármán			
P-O	1.534	871.3	-8.1
Lu-O	2.258	177.8	-23.0
Lu-O	2.354	123.5	-14.0
O-O	2.404	119.5	-28.2
O-O	2.553	81.3	-20.7
O-O	2.745	9.6	3.3
O-O	2.910	12.5	0.3
Shell-core			
O		2740	
Charges			
	Ionic	Shell	
O	-1.19	-2.68	
P	2.33	0	
Lu	2.44	0	

perfect crystal whereas the powder consists of micron-size crystalline grains. It does not consider the typical microstructure in a powder or atomic disorder in the grain-boundary region.

V. DISCUSSION

Since the shell model provides a consistent interpretation of the observed phonon-dispersion relations, DOS, Raman and IR data, and elastic constants of LuPO $_4$, we are confident that it is capable of describing the basic lattice excitations and thermodynamic properties characteristic of nonmagnetic xenotime-structure host compounds. If Lu is partly or fully replaced by another magnetic rare-earth element, the splitting of the Hund's-rule ground multiplet of the paramagnetic ions by the crystalline electric fields will give rise to a distinct set of levels. It has been found that for all the magnetic rare-earth ions in the xenotime series the crystal-field splitting of the ground multiplet is of the order of 40 meV and, therefore, overlaps the phonon energies for the rare-earth motion (see the Lu partial DOS in Fig. 5). Depending on the symmetry properties of the phonon and crystal-field states, interactions of the magnetic and lattice systems may take

TABLE VII. Elastic constants of LuPO $_4$.

Elastic constant	Measured ^a (10^{12} dyn/cm 2)	Calculated (10^{12} dyn/cm 2)
C_{11}	3.20(3)	3.31
C_{12}	0.36(7)	0.29
C_{13}	1.15(5)	1.24
C_{33}	3.82(14)	3.97
C_{44}	0.846(8)	0.831
C_{66}	0.217(2)	0.156

^aReference 22.

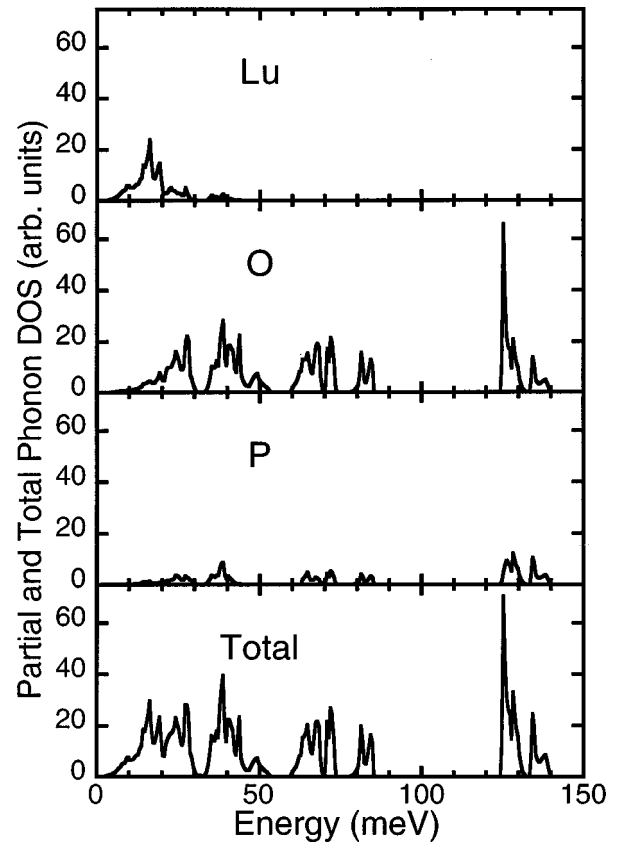


FIG. 5. Partial phonon density of states (PDOS) calculated from the shell model.

place—usually at low temperatures. For example, a cooperative Jahn-Teller effect occurs in TbPO $_4$ at about 2 K involving Tb ion-lattice coupling that induces a tetragonal-to-monoclinic distortion of the crystal lattice and a readjustment of the Tb electronic states.²⁶ In YbPO $_4$, coupling between the low-lying electronic states of the Yb $^{3+}$ ions and a B_{1g} lattice strain mode gives rise to a $\sim 20\%$ softening of the $(C_{11} - C_{12})/2$ elastic constants at $T < 100$ K.²⁷ The exact nature of these spin-lattice interactions is not yet understood. We expect to find anomalous phonon behavior in certain (Q, E) regions in those RPO $_4$ members which exhibit strong $4f$ electron-phonon coupling. Such anomalies were, in fact, found in TbVO $_4$ and TmVO $_4$.^{5,28,29} Therefore, further studies of the low-lying phonon branches in compounds such as YbPO $_4$ and TbPO $_4$ in comparison with LuPO $_4$ are desirable.

Phonons above 40 meV involve mainly P and O motions. There are two disconnected PO $_4$ tetrahedra in the primitive cell. The relatively sharp features in both the P and O partial DOS around 40, 60–73, 80–86, and 120–140 meV suggest that the force fields around the two PO $_4$ units are similar and the P and O atoms in each unit vibrate almost independently. The large gap separates the low-energy O-P-O bending modes from the high-energy P-O stretch vibrations. There are eight stretch modes resulting in two sharp peaks at about 128 and 135 meV (see Figs. 4–6), which may be related to the asymmetric-type and symmetric-type P-O stretches, respectively. If the PO $_4$ tetrahedra are linked by sharing one or more common O atoms, direct interactions of the tetrahedra will lead to more correlated motions. In addition, energy minimization under these geometries causes a distribution of

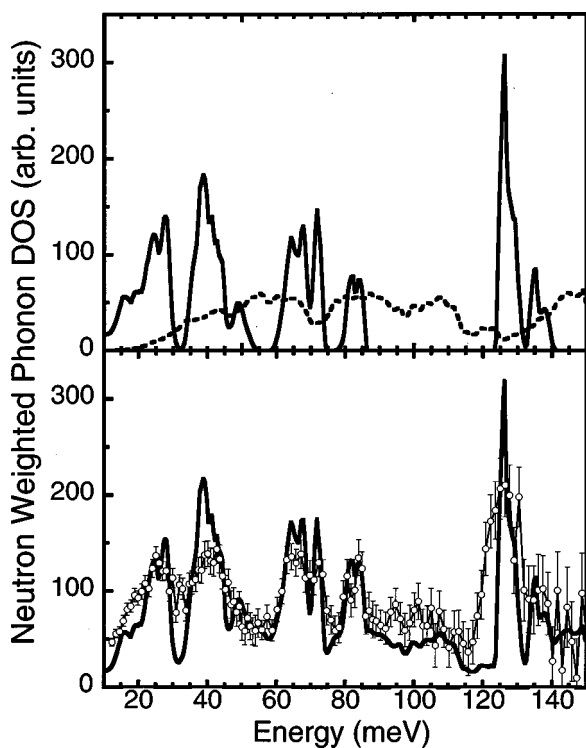


FIG. 6. Measured (open circles) and calculated (lines) generalized phonon density of states for LuPO_4 . The calculated two-phonon density of states is given as the dashed line in the top panel.

P-O bond lengths. Consequently, as the P and O phonon bands broaden, the size of the phonon band gap decreases. This trend has been observed in rare-earth ultraphosphates and pyrophosphates. In the extreme cases of pure crystalline or glassy P_2O_5 in which a three-dimensional network of PO_4 tetrahedra is formed, the P-O stretch vibrations spread to reveal several phonon bands and extend to a considerable higher energy of ~ 160 meV. This large increase of P-O stretch frequencies is related to the resonance of the additional P $d\pi$ -O $p\pi$ bonding among the four P-O σ bonds, a concept proposed by Pauling.

Finally, the lattice specific heat of LuPO_4 can be evaluated using the phonon DOS predicted by the shell model. Figure 7 shows the specific heat obtained and the Debye temperature as a function of temperature. The Debye temperature extrapolated to 0 K, Θ_0 , is ~ 500 K (see inset of Fig. 7). This relatively high Θ_0 indicates a high stiffness of the lattice at low temperature. The slow saturation of the specific heat at temperatures over 1000 K is the result of the high phonon cutoff energy. To the best of our knowledge, the specific heat of LuPO_4 has not yet been measured. However, the specific heat of isostructural nonmagnetic ScPO_4 was reported over the temperature range of 300–1600 K.^{30,31} The experimental values of the specific heat at constant pressure for ScPO_4 are compared to the calculated specific heat at constant volume for LuPO_4 in Fig. 7. The agreement is very good over the temperature range of the measurement where the increase of the specific heat arises mainly from high-energy phonons. Additionally, the specific heat for several other $R\text{PO}_4$ compounds (e.g., TbPO_4 and DyPO_4) were

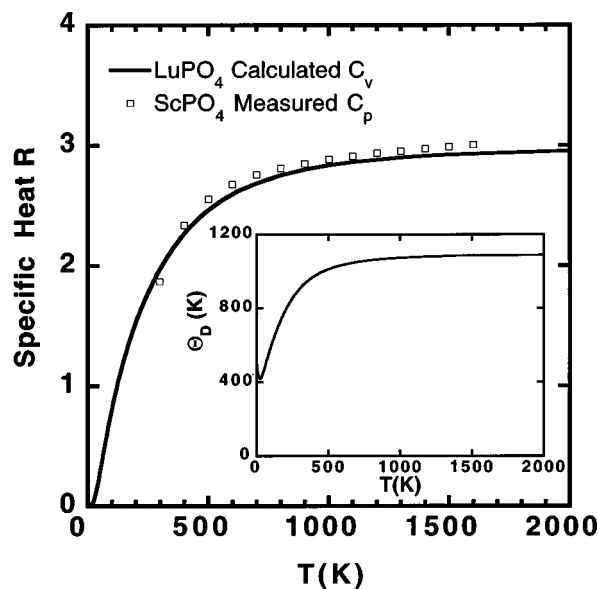


FIG. 7. The calculated lattice specific heat in terms of R per average atom (R is universal gas constant) at constant volume (solid line) for LuPO_4 and measured specific heat at constant pressure for ScPO_4 (\square). The calculated temperature dependence of the Debye temperature for LuPO_4 is plotted in the inset.

determined at low temperatures in association with studies of magnetic phase transitions.^{32,33} In those cases, the measured specific heat is a sum of magnetic and lattice contributions. To a large extent, the component of the lattice specific heat can be approximated by that of LuPO_4 . Therefore, the present result is useful for estimating the paramagnetic specific heat in many $R\text{PO}_4$ compounds.

In summary, we have measured the major phonon-dispersion curves and the phonon DOS of the nonmagnetic end member of the xenotime series, LuPO_4 , by neutron spectroscopy. A shell model was applied to the interpretation of the lattice-dynamic data. After optimization, a set of parameters was obtained which permitted a quantitative understanding of the neutron results as well as optical data and elastic constants given previously for LuPO_4 in the literature. The present study has provided the basic information regarding the phonon and thermodynamic properties of zircon-type structures. The result provides a basic reference for further investigations of spin-lattice interactions in the magnetic $R\text{PO}_4$ compounds and for comparisons with phosphorus and oxygen motions in different condensed phosphate materials.

ACKNOWLEDGMENTS

This work was partly provided by a NATO Collaborative Research Grant No. CRG940096. Work performed at Argonne National Laboratory and Oak Ridge National Laboratory is supported by the U.S. DOE-BES under Contracts No. W-31-109-ENG-38 and No. DE-AC05-96OR22464, respectively. The experiments performed at the Laboratoire Leon Brillouin (CE-Saclay) were supported by HCM program Access to Large Scale Facilities under Contract No. ERB CHGECT920001.

- ¹J. O. Nriagu, P. B. Moore, and F. Betts, *Phosphate Minerals* (Springer-Verlag, Berlin, 1984).
- ²E. W. J. L. Oomen, W. M. A. Smit, and G. Blasse, *Phys. Rev. B* **37**, 18 (1987).
- ³R. T. Harley, in *Spectroscopy of Solids Containing Rare Earth Ions*, edited by A. Kapyanskii and R. M. Macfarlane (Elsevier, Amsterdam, 1987), p. 557.
- ⁴G. A. Gehring and K. A. Gehring, *Rep. Prog. Phys.* **38**, 1 (1975).
- ⁵J. K. Kjems, W. Hayes, and S. H. Smith, *Phys. Rev. Lett.* **35**, 1089 (1975).
- ⁶S. W. Martin, *Eur. J. Solid State Inorg. Chem.* **28**, 163 (1991).
- ⁷J. R. Van Wazer, *Phosphorus and its Compounds* (Interscience, New York, 1958), Vol. I.
- ⁸A. Armbruster, *J. Phys. Chem. Solids* **37**, 321 (1976).
- ⁹P. C. Becker, Ph.D. thesis, Lawrence Berkeley Laboratory, University of California, Berkeley, 1986.
- ¹⁰G. M. Begun, G. W. Beall, L. A. Boatner, and W. J. Gregor, *J. Raman Spectrosc.* **11**, 273 (1981).
- ¹¹A. N. Lazarev, N. A. Mazhenov, and A. P. Mirgorodskii, *Izv. Akad. Nauk SSSR, Neorg. Mater.* **14**, 2107 (1978).
- ¹²E. N. Yurchenko, E. B. Burgina, V. I. Bugakov, E. V. Murav'ev, V. P. Orlovskii, and T. V. Belyaevskaya, *Izv. Akad. Nauk SSSR, Neorg. Mater.* **14**, 2038 (1978).
- ¹³I. Richman, *J. Opt. Soc. Am.* **56**, 1589 (1966).
- ¹⁴P. Dawson, M. M. Hargreave, and G. R. Wilkinson, *J. Phys. C* **4**, 240 (1971).
- ¹⁵R. W. Mooney and S. Z. Toma, *J. Chem. Phys.* **46**, 3364 (1967).
- ¹⁶S. A. Miller, H. H. Caspers, and H. E. Rast, *Phys. Rev.* **168**, 964 (1967).
- ¹⁷W. O. Milligan, D. F. Mullica, G. W. Beall, and L. A. Boatner, *Acta Crystallogr., Sect. C* **39**, 23 (1983).
- ¹⁸G. Venkataraman, L. A. Feldkamp, and V. C. Sahni, *Dynamics of Perfect Crystals* (MIT Press, Cambridge, MA, 1975).
- ¹⁹G. Herzberg, *Infrared and Raman Spectra of Polyatomic Molecules* (Van Nostrand, Princeton, New Jersey, 1964).
- ²⁰M. Rappaz, L. A. Boatner, and M. M. Abraham, *J. Chem. Phys.* **73**, 1095 (1980).
- ²¹M. M. Abraham, L. A. Boatner, T. C. Quinby, D. K. Thomas, and M. Rappaz, *Radioactive Waste Management* **1**, 181 (1980).
- ²²A. Armbruster, R. Thomä, and H. Wehrle, *Phys. Status Solidi A* **24**, K71 (1974).
- ²³D. L. Price and K. Sköld, in *Neutron Scattering*, edited by K. Sköld and D. L. Price (Academic, Orlando, 1986), Vol. A, p. 29.
- ²⁴V. S. Oskotskii, *Fiz. Tverd. Tela (Leningrad)* **9**, 550 (1967) [*Sov. Phys. Solid State* **9**, 420 (1967)].
- ²⁵M. M. Bredov, B. A. Kotov, N. M. Okuneva, V. S. Oskotskii, and A. L. Shakh-Budagov, *Fiz. Tverd. Tela (Leningrad)* **9**, 287 (1967) [*Sov. Phys. Solid State* **9**, 214 (1967)].
- ²⁶P. Morin, J. Rouchy, and Z. Kazei, *Phys. Rev. B* **50**, 12 625 (1994).
- ²⁷J. Nipko, M. Grimsditch, C.-K. Loong, S. Kern, M. M. Abraham, and L. A. Boatner, *Phys. Rev. B* **53**, 2286 (1996).
- ²⁸M. T. Hutchings, R. Scherm, and S. R. P. Smith, in *Proceedings of the 21st Annual Conference on Magnetism and Magnetic Materials*, edited by J. J. Becker, G. H. Lander, and J. J. Rhyne, AIP Conf. Proc. No. 29 (AIP, New York, 1976).
- ²⁹R. J. Elliott, R. T. Harley, W. Hayes, and S. R. P. Smith, *Proc. R. Soc. London, Ser. A* **328**, 217 (1972).
- ³⁰D. Sh. Tsagareichvili, G. G. Gvelesiani, V. P. Orlovskii, T. V. Belyaevskaya, and V. P. Repko, *Izv. Akad. Nauk SSSR, Neorg. Mater.* **8**, 1790 (1972).
- ³¹D. Sh. Tsagareichvili, G. G. Gvelesiani, V. P. Orlovskii, and T. V. Belyaevskaya, *Izv. Akad. Nauk SSSR, Neorg. Mater.* **11**, 491 (1975).
- ³²R. W. Hill, J. Cosier, and S. H. Smith, *Solid State Commun.* **26**, 17 (1978).
- ³³J. H. Colwell, B. W. Mangum, and D. D. Thornton, *Phys. Rev. Lett.* **23**, 1245 (1969).